ChemistrySelect

Research Article
doi.org/10.1002/slct.202201504

Chemistry Europe
European Chemical Societies Publishing

www.chemistryselect.org

Structural and Molecular Packing study of Three New Amidophosphoric Acid Esters and Assessment of Their Inhibiting Activity Against SARS-CoV-2 by Molecular Docking

Nafiseh Heidari,[a] Atekeh Tarahhomi,*[a] and Arie van der Lee[b]

Three new compounds of amidophosphoric acid esters with a $[OCH_2C(CH_3)_2CH_2O]P(O)[X]$ segment (where X = cyclopentylamido (**1**), 2-aminopyridinyl (**2**) and pyrrolidinyl (**3**)) were synthesized and studied using FT-IR and $^{31}P/^{13}C/^{1}H$ NMR spectroscopies and single-crystal X-ray diffraction analysis. The compounds crystallize in the triclinic space groups $P\bar{1}$ for **1** and **3** and in the orthorhombic space group $Pca2_1$ for **2**, where the asymmetric unit consists of three symmetrically-independent molecules for **1** and one molecule for **2** and **3**. The intermolecular interactions and supramolecular assemblies are assessed by Hirshfeld surface analysis and enrichment ratios. The results reveal that the substituent effect plays an important role in directing the supramolecular structures. The presence of the aromatic substituent aminopyridine in **2** providing the C–H…π interactions leads to a larger variety in interactions including H…H, H…O/O…H, H…C/C…H and H…N/N…H contacts, whereas the packings of the compounds **1** and **3** bearing aliphatic substituents only include H…H and H…O/O…H contacts. The enrichment ratios affirm the importance of O…H/H…O contacts reflecting the hydrogen bond N–H…O interactions to be the enriched contacts. Compounds **1–3** were also investigated along with five similar reported structures with a $[OCH_2C(CH_3)_2CH_2O]P(O)$ segment for their inhibitory behavior against SARS-CoV-2. The molecular docking results illustrate that the presence of the aromatic amido substituent *versus* the aliphatic type provides a more favorable condition for their biological activities.

Introduction

Amidophosphoric acid esters are attractive as bioactive agents due to their structural properties allowing them to interact with various living systems. They can be employed as nucleotide prodrugs and antitumor, anticancer or antiviral agents.[1–4] The design of new materials with biological applications requires a suitable insight of various intermolecular interactions within a biotic environment such as an active site of an enzyme.[5] In the context of this study it is of relevance that amidophosphoric acid esters can inhibit urease and acetylcholinesterase enzymes.[6,7]

The Severe Acute Respiratory Syndrome Coronavirus 2 (SARS-CoV-2) has since its appearance in 2019 attracted extensive research towards the development of effective medication against its consequences on human health, but no approved and decisive drug is known until now to treat this virus.[8,9] Clinical trials of new anti-coronavirus drugs request a long time and equipment; therefore computer-aided drug discovery such as molecular docking simulation which tests the binding interactions between the target protein of virus and the tested drug compound are being used to evaluate the activity of a drug and to accelerate the choice of potential drugs for clinical trials.[10,11] Some suitable antiviral drugs based on phosphoramides and phosphonates such as Tenofovir, Sofosbuvir and Remdesivir have been proposed as anti-coronavirus agent.[12–15] Moreover, some phosphates-based compounds were suggested as possible inhibitors against SARS-CoV-2.[16] There are, however, no reports of amidophosphoric acid esters as a sub-class of phosphoramides to evalute their inhibitory effect on coronavirus.

The investigation of various intermolecular interactions of potential drug compounds is of paramount importance to identify the key interactions between the target biological molecular structure and that of the drug compound.[17,18] The various intermolecular interactions in the structures of amidophosphoric acid esters have been investigated before in the presence or absence of N–H…O hydrogen bond.[19,20] The formation of 3D architectures in their molecular aggregations *via* weak interactions such as π-effects contacts and non-covalent forces has also been considered.[19,21]

With this insight in mind, we present in this study the structures of three new amidophosphoric acid esters, $[OCH_2C(CH_3)_2CH_2O]P(O)[X]$, ($X$=$HNC_5H_9$ (**1**), NHC_5H_4N (**2**) and NC_4H_8 (**3**)) (Scheme 1) determined from single-crystal X-ray crystallography. The spectroscopic properties of these compounds are investigated by FT-IR and $^{1}H/^{13}C/^{31}P$-NMR spectroscopy. The various intermolecular interactions and features of the supramolecular assemblies are examined by 3D Hirshfeld surface maps and 2D fingerprint plots along with the calculated

[a] *N. Heidari, Dr. A. Tarahhomi*
Department of Chemistry, Semnan University,
Semnan 35131-19111, Iran
E-mail: tarahhomi.at@semnan.ac.ir
[b] *Dr. A. van der Lee*
IEM, Université de Montpellier,
CNRS, ENSCM, Montpellier, France

Supporting information for this article is available on the WWW under https://doi.org/10.1002/slct.202201504

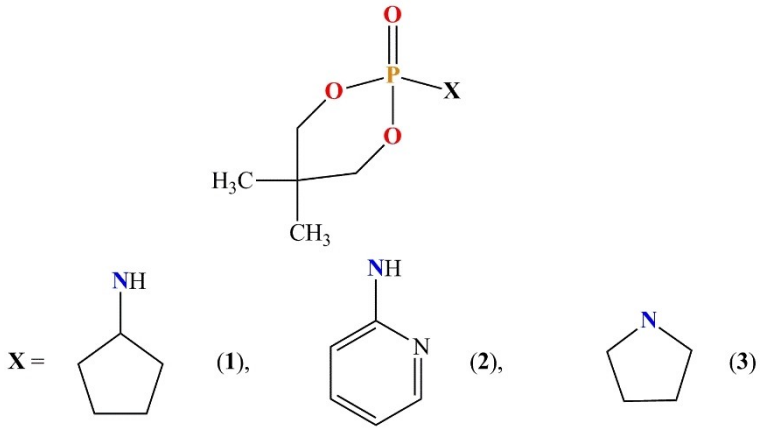

Scheme 1. Chemical structures of compounds **1–3**.

enrichment ratios. This allows us to give a detailed evaluation of the types of interactions and forces which stabilize the structures. Furthermore, a molecular docking study is presented to investigate the inhibitory effect of **1–3** and five similar compounds including the same $[OCH_2C(CH_3)_2CH_2O]P(O)$ segment against the coronavirus (Main Protease (M^{Pro}) of SARS-C_OV-2, 6M03).

Results and discussion

X-ray crystallography investigations

The compounds crystallize in the triclinic space group $P\bar{1}$ for **1** and **3** and in the orthorhombic space group $Pca2_1$ for **2**. Details of the crystallographic analyses are summarized in Table 1. The asymmetric unit has three molecules P1, P16 and P31 in **1** (Figure 1) and one entire molecule in **2** and **3** (Figure 2). The phosphorous atom has in all structures a distorted tetrahedral

Table 1. Crystal data and structure refinement for compounds **1–3**.

Compound	**1**	**2**	**3**
CCDC number	2110733	2110734	2110735
Chemical formula	$C_{10}H_{20}NO_3P$	$C_{10}H_{15}N_2O_3P$	$C_9H_{18}NO_3P$
M_r (gr/mol)	233.24	242.22	219.22
Temperature (K)	299	299	300
Crystal system, Space group	Triclinic, $P\bar{1}$	Orthorhombic, $Pca2_1$	Triclinic, $P\bar{1}$
a, b, c (Å)	11.5899 (6), 12.0785 (6), 14.9427 (7)	11.0062 (3), 12.6989 (4), 8.8257 (3)	6.4555 (4), 9.5793 (9), 9.6429 (8)
α, β, γ (°)	74.133 (4), 74.025 (4), 69.827 (5)	90, 90, 90	104.041 (7), 91.489 (6), 100.067 (6)
V (Å^3)	1850.36 (17)	1233.54 (7)	568.12 (8)
Z	6	4	2
Radiation type	Mo $K\alpha$	Mo $K\alpha$	Mo $K\alpha$
μ (mm^{-1})	0.21	0.22	0.23
$F(000)$	756	512	236
Crystal size (mm)	0.35×0.25×0.20	0.21×0.20×0.15	0.45×0.33×0.22
Crystal color/habit	Colorless/Prism	Colorless/Prism	Colorless/Prism
Diffractometer	Xcalibur, Sapphire3, Gemini	Xcalibur, Sapphire3, Gemini	Xcalibur, Sapphire3, Gemini
Theta range for data collection (°)	1.976 to 28.308	2.440 to 27.987	2.278 to 26.671
Absorption correction	Multi-scan/*CrysAlisPRO*	Multi-scan/CrysAlis*PRO*	Multi-scan/CrysAlis*PRO*
T_{min}, T_{max}	0.797, 1.000	0.952, 1.000	0.816, 1.000
No. of measured, independent and observed [$I > 2.0\sigma(I)$] reflections	45204, 9075, 7006	16957, 3010, 2726	7089, 2669, 2053
R_{int}	0.044	0.040	0.050
$(\sin\theta/\lambda)_{max}$ (Å^{-1})	0.683	0.684	0.682
$R[F^2 > 2\sigma(F^2)]$, $wR(F^2)$, S	0.063, 0.151, 1.07	0.029, 0.057, 1.11	0.058, 0.162, 1.07
No. of reflections	9075	3010	2669
No. of parameters	439	190	137
No. of restraints	0	1	0
H-atom treatment	H-atom parameters constrained	H-atom parameters constrained	H atoms treated by a mixture of independent and constrained refinement
$\Delta\rho_{max}$, $\Delta\rho_{min}$ (e.Å^{-3})	0.48, −0.40	0.14, −0.18	0.41, −0.30
Absolute structure parameter	–	−0.01 (4)	–

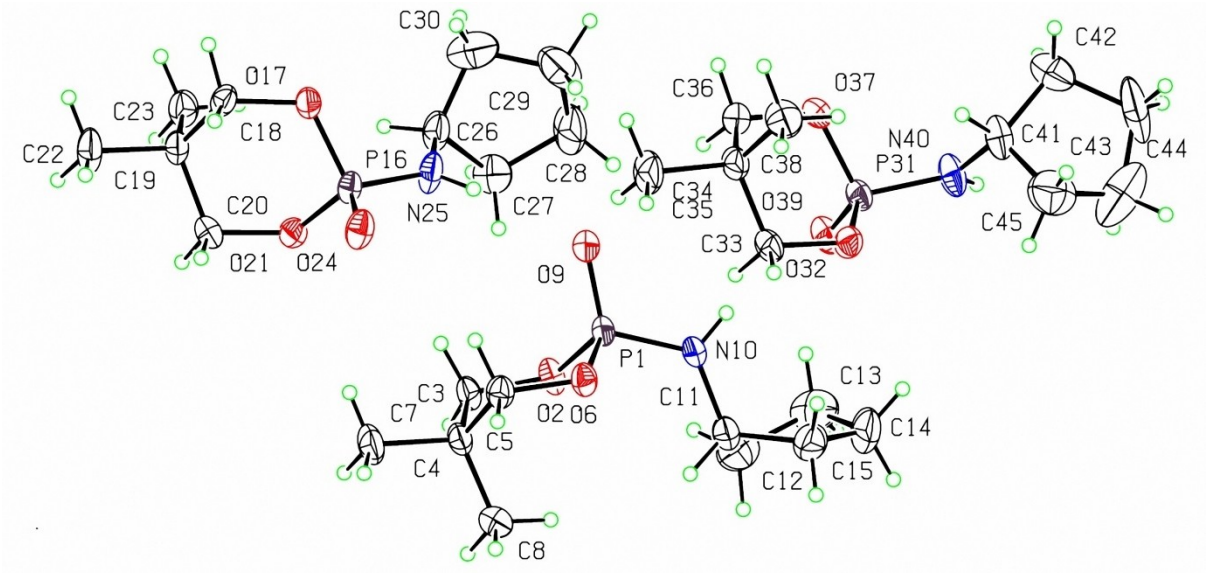

Figure 1. A view of the asymmetric unit of **1**, showing three independent molecules P1, P16 and P31 with the atom-labelling. Displacement ellipsoids are drawn at the 30% probability level and H atoms are drawn as circles of arbitrary radii.

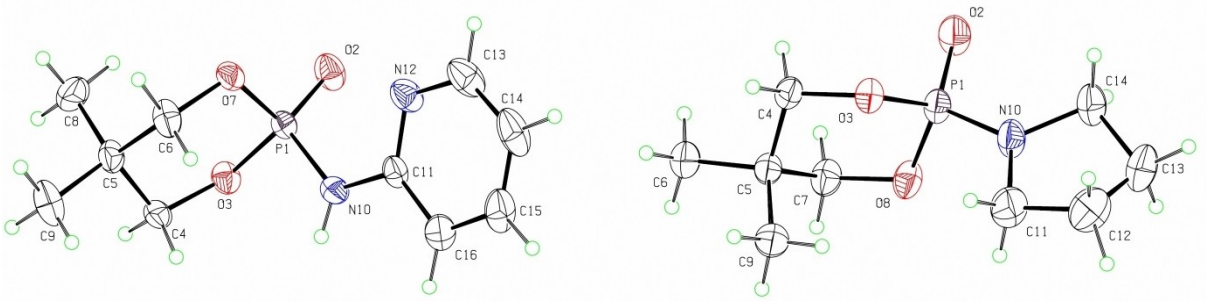

Figure 2. Views of Ellipsoid-style and atom-labeling presentation of molecular structures of **2** (left) and **3** (right) in the asymmetric unit. The 30% probability level has been allocated for drawing displacement ellipsoids and H atoms are drawn as circles of arbitrary radii.

O=P[–O]$_2$[–N] environment as evidenced from the bond lengths and angles around the P atom (Table S1), being in the same range as in the structures of similar amidophosphoric acid esters[19,20]

The sums of the surrounding angles at the N atoms (∠P–N–C + ∠C–N–H + ∠P–N–H) in compounds **1** and **2** are slightly deviating from zero: 0.06, 0.03 and 0.21°, for P1, P16 and P31 in **1**, and 0.03° in **2** from establishing a mainly sp^2 hybridization for these secondary amines. For compound **3**, the sum of the surrounding angles at the tertiary N atom (∠P–N–C + ∠P–N–C + ∠C–N–C) being 359.99 (18)° confirms a sp^2 character and a planar configuration of this N atom. Such secondary (in **1** and **2**) and tertiary (in **3**) nitrogen atoms which display a low Lewis-base character cannot play a role as an acceptor in any hydrogen bond interaction.

In all structures **1–3**, the six-membered ring of the same [OCH$_2$C(CH$_3$)$_2$CH$_2$O]P(O) segment adopts a nearly-chair conformation. For **2**, the P=O bond of this ring is located in an equatorial position (with angles $O_{P=O}$–P–O_{estric} = 110.92 (7)° and 112.24 (6)°,$O_{P=O}$–P–N = 116.16 (7)° and O_{estric}–P–N = 102.66 (6)° and 108.80 (6)°), whereas for **1** ($O_{P=O}$–P–O_{estric} = 113.01 (10)° and 114.93 (10)°,$O_{P=O}$–P–N = 114.79 (10)° and O_{estric}–P–N = 104.98 (10)° and 105.71 (10)° for the molecule P1) and **3** ($O_{P=O}$–P–O_{estric} = 114.80 (10)° and 114.03 (10)°,$O_{P=O}$–P–N = 113.75 (10) ° and O_{estric}–P–N = 105.24 (10)° and 105.33 (11) °), the P=O bond position is intermediate between equatorial and axial. The equatorial position of the P=O bond in **2** may be attributed to the *near anti*-orientation of the N–H unit relative to the P=O group and the endo anomeric effect[22] *via* the *n* (the non-bonding orbital of the endocyclic N atom) to σ^* (the anti-bonding orbital of P–$N_{exocyclic}$) overlap, as such position of the P=O bond has been observed in the similar diazaphosphorinane ring.[23] In the structures **1** and **2**, where the favoured interactions in phosphoramides, i. e. classical N–H…O=P hydrogen bond interaction, are present, a linear framework as a 1D chain building *C*(4) motif is formed along the [010] and [001] axis, respectively (Table 2, Figure 3). The different *syn*- (in **1**) and *near anti* (in **2**)-orientations of the N–H unit relative to the

Table 2. Hydrogen bond geometry (Å, °) for compounds **1–3**.

D–H···*A*	*D*–H	H···*A*	*D*···*A*	*D*–H···*A*
1				
N10–H10···O39=P31	0.85 (3)	2.13 (2)	2.958 (3)	165 (3)
N25–H25···O9=P1	0.85 (3)	2.14 (3)	2.964 (3)	163 (3)
N40–H40···O24=P16^{i}	0.86 (4)	2.08 (4)	2.920 (4)	167 (3)
C20–H20b···O39=P31^{ii}	1.06 (2)	2.58 (2)	3.576 (4)	156 (6)
C5–H5a···O6^{iii}	1.06 (2)	2.61 (1)	3.509 (3)	142 (5)
C5–H5b···O24=P16	1.06 (1)	2.60 (1)	3.612 (3)	158 (8)
H13a…H38b^{iv}		2.11 (3)		
2				
N10–H10··· O2=P1^{i}	0.99 (2)	1.86 (2)	2.841 (2)	171 (1)
C9–H9 A···O3^{ii}	1.05 (3)	2.48 (3)	3.514 (3)	168 (2)
C4–H4B···O2=P1^{ii}	1.06 (2)	2.63 (2)	3.525 (2)	142 (1)
C8–H8B···O2=P1^{i}	1.02 (2)	2.62 (2)	3.607 (3)	161 (2)
C14–H14···O7^{iii}	1.03 (2)	2.52 (2)	3.284 (2)	130 (2)
C13–H13···π	–	2.979	–	128
C6–H6 A···π	–	2.931	–	162
3				
C6–H6b···O2=P1^{i}	1.10 (1)	2.43 (1)	3.421 (3)	149 (1)
C4–H4a···O2=P1^{ii}	1.07 (1)	2.43 (1)	3.491 (3)	173 (5)
C4–H4b···O2=P1^{i}	1.06 (1)	2.43 (1)	3.407 (2)	151 (8)

Symmetry transformations used to generate equivalent atoms for **1**: (i) *x*, *y*–1, *z*, (ii) *x*, *y*+1, *z*, (iii) −*x*, −*y*+1, −*z*+1, (iv) *x*–1, *y*, *z*; for **2**: (i) −*x*+1, −*y*+1, *z* - $\frac{1}{2}$; (ii) −*x*+$\frac{1}{2}$, *y*, *z*–$\frac{1}{2}$, (iii) *x*–$\frac{1}{2}$, −*y*+2, *z*; for **3**: (i) −*x*+1, −*y*, −*z*; (ii) *x*+1, *y*, *z*.

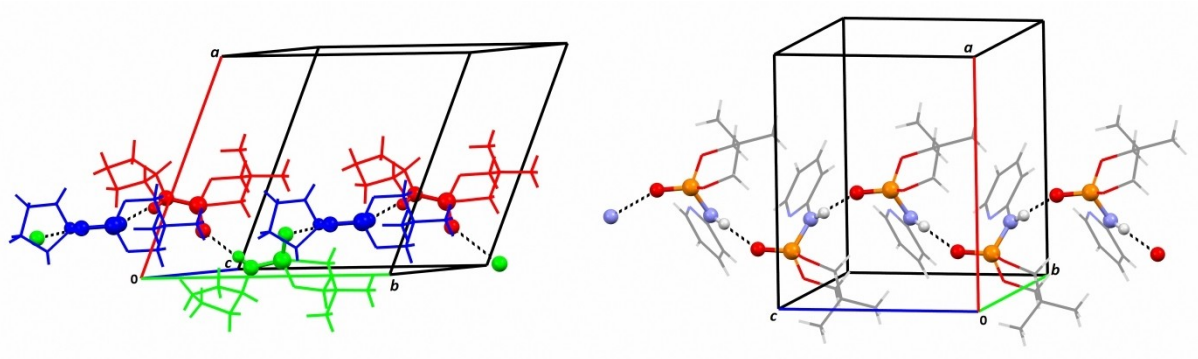

Figure 3. Partial views of the molecular packings of **1** (left) and **2** (right) formed *via* classical N–H…O=P hydrogen bond. The 1D linear arrangement along the *b* (for **1**) and *c* (for **2**) axis are formed. For **1**, the 1D chain is produced by linking of three symmetry-independent molecules shown by different colors (red, blue and green). The O=P–NH segments involved in hydrogen bonding are shown as 'ball and sticks'.

P=O group form a similar molecular zigzag type arrangement for these 1D chains. However, in the case of **1**, the 1D chain is built up by linking three neighbouring symmetry-independent molecules P1, P16 and P31. This molecular packing formed by the classical N–H…O=P hydrogen bond interaction in **1** and **2** is not found in the structure of **3**. Indeed, the oxygen atom of the phosphoryl group in **3** serves as a strong hydrogen-bonding acceptor. However, all hydrogen atoms are part of methyl and methylene groups and these are consequently the only available hydrogen-bonding donors which are much weaker than the classical hydrogen-bond donors. Therefore, in the absence of the favoured donor unit in phosphoramides, i.e. the N–H unit, not any classical hydrogen bond interaction is found in the structure of **3**.

Study of the intermolecular interactions and packing features by Hirshfeld surface (HS) analysis

The supramolecular features of the structures **1–3** are studied by using Hirshfeld surface analysis,[13,33] an easy-to-operate graphical tool to visually investigate various intermolecular interactions in molecular crystal structures. The graphical 3D Hirshfeld surfaces (HSs) mapped over the d_{norm} parameter and the derived 2D fingerprint plots (FPs) for **1–3** are illustrated in Figures 4 –6 and S1, S2, S3. For **2**, the HS mapped over the shape index property is shown in Figure 5. The intermolecular contacts and their contribution percentages are also reported in Table 3.

The characteristic red spots near the oxygen atom of the P=O group and the hydrogen atom of the N–H unit in the

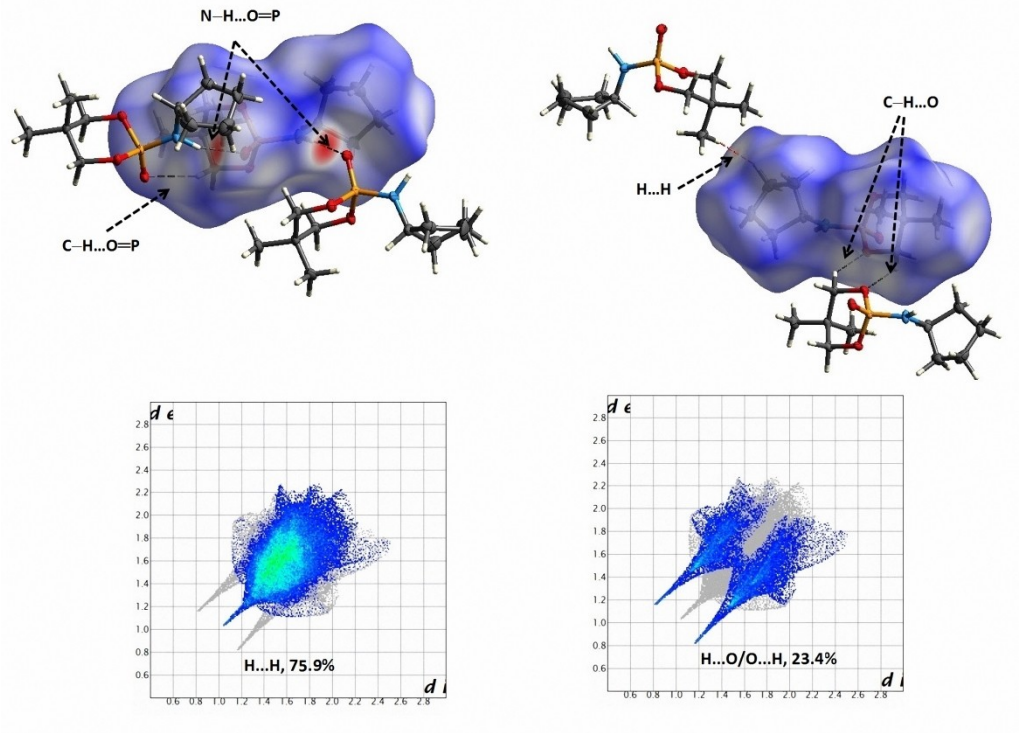

Figure 4. Views of the d_{norm} Hirshfeld surface maps (up) plotted on the molecule P1 of **1** in two orientations, introducing close contacts, along with the H…H and H…O/O…H fingerprint plots (down).

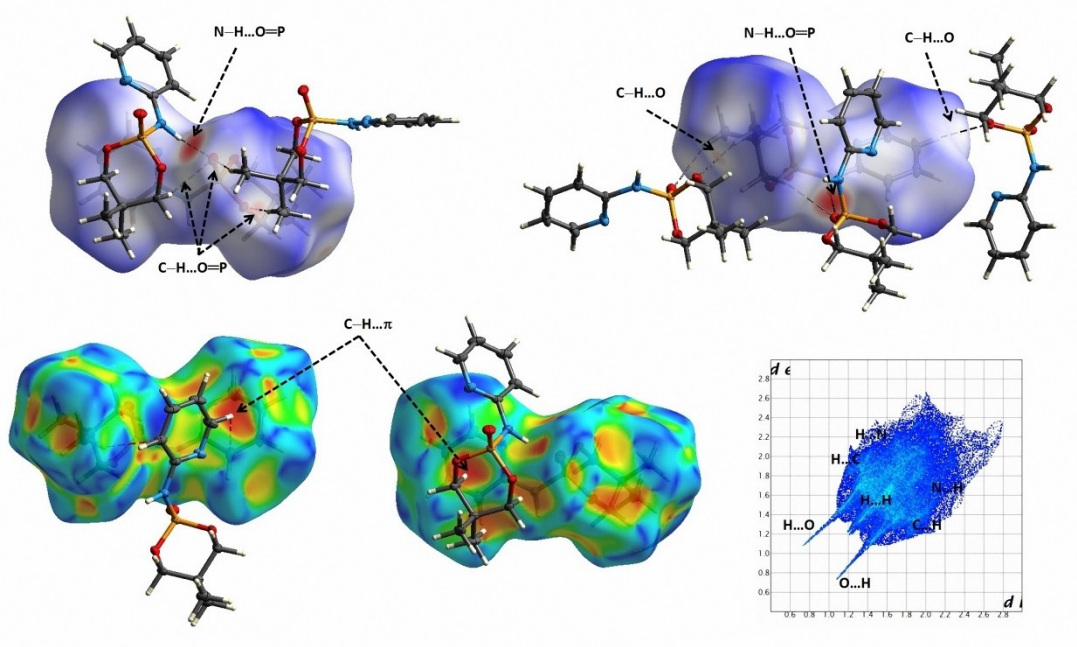

Figure 5. Views of the d_{norm} Hirshfeld (up) and shape index (down) surface maps plotted on the compound **2** in two orientations, introducing close contacts, along with the full fingerprint plot labeling features related to the main intermolecular contacts (down).

Hirshfeld surface of the structures **1** and **2** confirm the previously mentioned N–H…O=P classical hydrogen bond. For the molecules P1 and P31 of **1**, some little bright red spots on white regions are also seen which are related to H…H contacts (Table 2). The weak C–H…O=P hydrogen bond interactions in **1** and **2** (Table 2) are represented as white regions, while for **2**,

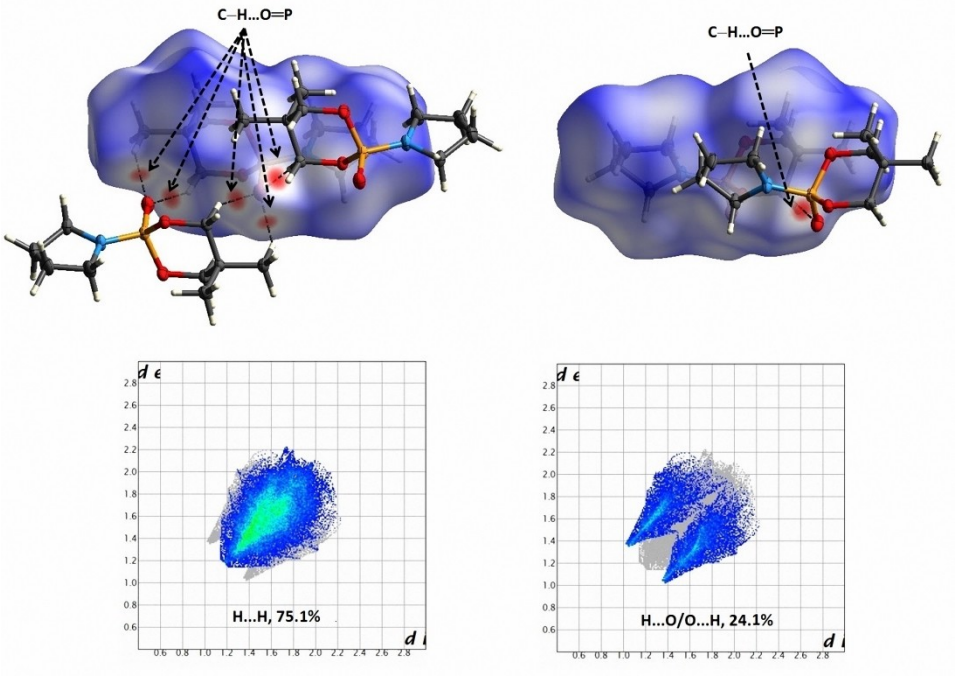

Figure 6. Views of the d_{norm} Hirshfeld surface maps (up) plotted on the compound **3** in two orientations, introducing close contacts, along with the H…H and H…O/O…H fingerprint plots (down).

Table 3. Data derived from Hirshfeld surface analysis for the compounds **1**–**3**. The numbers refer to the contribution (in percentage) to the Hirshfeld surface area of the various intermolecular contacts. Contacts with percentage lower than unity are not included.

Contacts	**P1 of 1**	**P16 of 1**	**P31 of 1**	**2**	**3**		S_X	H	O	C	N
H…H	75.9	73.1	78.0	53.7	75.1		**P1**	87.60	11.70	–	–
H…O/O…H	23.4	26.4	21.4	24.8	24.1		**P16**	86.30	13.20	–	–
H…C/C…H	–	–	–	13.4	–		**P31**	88.70	10.70	–	–
H…N/N…H	–	–	–	7.6	–		**2**	76.60	12.40	6.70	3.80
							3	87.15	12.05	–	–
Atoms		H	O			H	O			H	O
P1 of 1	R_{XX}/R_{XY}			**P16 of 1**	R_{XX}/R_{XY}			**P31 of 1**	R_{XX}/R_{XY}		
H		76.74	20.50	H		74.48	22.78	H		78.68	18.98
O		20.50	–	O		22.78	–	O		18.98	
P1 of 1	E_{XX}/E_{XY}			**P16 of 1**	E_{XX}/E_{XY}			**P31 of 1**	E_{XX}/E_{XY}		
H		0.99	1.14	H		0.98	1.16	H		0.99	1.13
O		1.14	–	O		1.16	–	O		1.13	–
2	R_{XX}/R_{XY}	H	O	C	N			**3**	R_{XX}/R_{XY}		
H		58.67	19.00	10.26	5.82			H		75.95	21.00
O		19.00	–	–	–			O		21.00	–
C		10.26	–	–	–						
N		5.82	–	–	–						
2	E_{XX}/E_{XY}							**3**	E_{XX}/E_{XY}		
H		0.91	1.31	1.31	1.31			H		0.99	1.15
O		1.31	–	–	–			O		1.15	–
C		1.31	–	–	–						
N		1.31	–	–	–						

some of these interactions visible as little pale-red spots stabilize the structure. In the case of **3**, in the absence of the classical N–H…O=P hydrogen bonds, the C–H…O=P hydrogen bond interactions play the important role in the stabilization of the molecular packing and are revealed as red spots. Moreover, for **2** bearing the aromatic substituent pyridine ring, the red π-hole features on the shape index surface (Figure 5) affirm the presence of π-effect interactions of the C–H…π type (Table 2).

In the FPs of **1** and **3**, the contributions originate only from H…H and H…O/O…H interactions, where the packing is dominated by H…H contacts, accounting for as high as 76.0% and 75.0% of the packing forces in **1** and **3**, respectively. The percentage contribution of H…O/O…H contacts to the packing

is 23.3% (for **1**) and 24.2% (for **3**). In the case of **2**, the largest contribution is found for the H…H contact (53.1%), followed by the H…O/O…H (25.1%), H…C/C…H (13.3%) and H…N/N…H (8.0%) interactions. The larger variety of contacts in **2**, including H…H, H…O/O…H, H…C/C…H and H…N/N…H interactions, compared with **1** and **3** having only H…H and H…O/O…H interactions, can be attributed to the presence of the aromatic substituent aminopyridine which provides the π-effect C–H…π interactions, i.e. H…C/C…H type contacts. Furthermore, this substituent bearing the nitrogen atom in aromatic ring gives rise to the H…N/N…H contacts.

The combined H…O/O…H contacts for **1** and **2** appear as large symmetrically sharp spikes with minimum values of $d_i + d_e \approx 2.0$ Å for **1** and 1.8 Å for **2**, whereas these spikes are small for **3** ($d_i + d_e \geq 2.4$ Å). This result can be attributed to the presence of the classical N–H…O=P hydrogen bond interaction providing the lowest values of $d_i + d_e$ in **1** and **2** *versus* the absence of such classical interaction in **3**. However, all such close H…O/O…H contacts in **1**–**3** are at values less than the sum of the van der Waals (vdW) radii of the oxygen and hydrogen atoms (≈2.7 Å). Moreover, the H…H contact in **1** leads to a sharp spike on the diagonal plot reflecting some short H…H contacts with $d_i + d_e \approx 2.0$ Å which are less than 2× the vdW radius of hydrogen atom (≈2.2 Å).

The wings at the top left and bottom right of the plot of **2** are related to a series of H…C/C…H contacts, while the fraction of these contacts to the packing is 13.3%. Other regions of the plot are occupied by the H…N/N…H contacts whose fraction to the total surface accounts for only 8.0%.

Enrichment ratio (E_{XY})

The propensity of pair atoms (X, Y) to form contacts can be assessed by calculating the enrichment ratios E_{XY} from the Hirshfeld surface fingerprint plots. For a high propensity the X…Y contact is recognized as favored when $E > 1$ and for a low propensity the interaction is disfavored when $E < 1$.[24,25] The enrichment ratios of the compounds **1–3** computed by the results derived from the HS analysis have been given in Table 3.

The results of the enrichment ratios analysis affirm the importance of O…H/H…O contacts including the classical N–H…O=P hydrogen bond interaction in the crystal packings of **1–3** for which these contacts are favored ($E_{OH} > 1$). In contrast, the H…H contacts are disfavored in all three compounds with $E_{HH} = 0.91$–0.99, where the lowest value of E_{HH} is found for **2**. As is mentioned above, the presence of the aromatic substituent in the structure of **2** supports the formation of the C…H/H…C and N…H/H…N contacts inside the H…H and O…H/H…O. The existence of such extra contacts in **2** compared with **1** and **3** can underestimate the importance of the H…H contacts in this structure to be completely disfavored. This is in line with the obtained results of the C…H/H…C and N…H/H…N ratios for **2** which are larger than unity (Table 3) and turn out to be enriched.

Molecular docking study

In order to predict the intermolecular framework formed between the studied compounds **1**–**3** and the target macromolecular structure generating a binding model, a molecular docking approach was employed. For this study, the small molecules **1**–**3** are docked into the target protein 6M03 (Figure 7) to calculate the energetic values at the binding sites, where 6M03 is one of the important proteins which plays a key role in the propagation of the coronavirus. The simulations were done on each of structures selecting the best pose of the compound toward the receptor from the ranking of different poses by the highest negative binding energy. The best ranking binding energies were computed as −6.35, −5.98 and −5.47 kcal/mol for **1–3**, respectively. The results show that all studied compounds give efficient binding energy with negative values. These obtained data confirm that the interaction of **1–3** with 6M03 can inhibit the activity of this protein and in result, could prevent the coronavirous function. Thus, amidophosphoric acid esters **1**–**3** are potential inhibitors of M^{Pro} of SARS-CoV-2 to be confirmed by in-vivo experiments.

Figures 7 and S4 display the various interactions between the compounds **1–3** and the structure of the 6M03 protein. For **1**, hydrogen bonding (HB) interactions are formed between the hydrogen atom of NH group and the oxygen atom of the esteric ring with the amino acid residues of GLU A166. The five-membered ring of amino substituent of **1** interacts with the MET A165, LEU A167 and PRO A168 binding sites. The carbon atoms of the esteric ring also interact with the amino acid residues of MET A165, MET A49, CYS A145, HIS A164 and HIS A41. For **2**, the oxygen atom and the carbon atom of the CH_3 group of the esteric ring are interacting with CYS A145. An interaction is also found between the aromatic pyridine ring with MET A165. Other observed interactions are formed between the HIS A163 with the CH_3 groups of the esteric ring. In the case of **3**, the obvious interactions are the HBs formed between the P=O oxygen atom with the LYS A5 and ARG A4 and between the esteric ring with the LEU A282, PHE A3, TRP A207 and PHE A291.

For a detailed investigation, we performed the docking simulations for the main protein of SARS-CoV-2 (6M03) on similar compounds **4–8** which have been previously reported[26,19,27] using the crystal structure data available in the Cambridge Structural Database (CSD). All these structures are in the family of the amidophosphoric acid ester with a same $[OCH_2C(CH_3)_2CH_2O]P(O)$ segment, but with different amino substitutions (Scheme 2). The goal is to investigate the effect of the amino substitions on the biological acivity of these such structures. The molecular docking figures of **1–8** are shown in Figs. S4 and S5, and the related data reported in terms of binding energy (kcal/mole) are summarized in Table 4.

The largest negative binding energies are found for compounds **1**, **2**, **4**, **5** and **8**, respectively, where for compounds **2** and **8**, the aromatic substituent comes into play in the amino segment. Compound **2** bearing the nitrogen atom at the aromatic pyridine ring has a slightly higher binding energy of 0.08 kcal/mole compared to that of **8**. The lowest negative

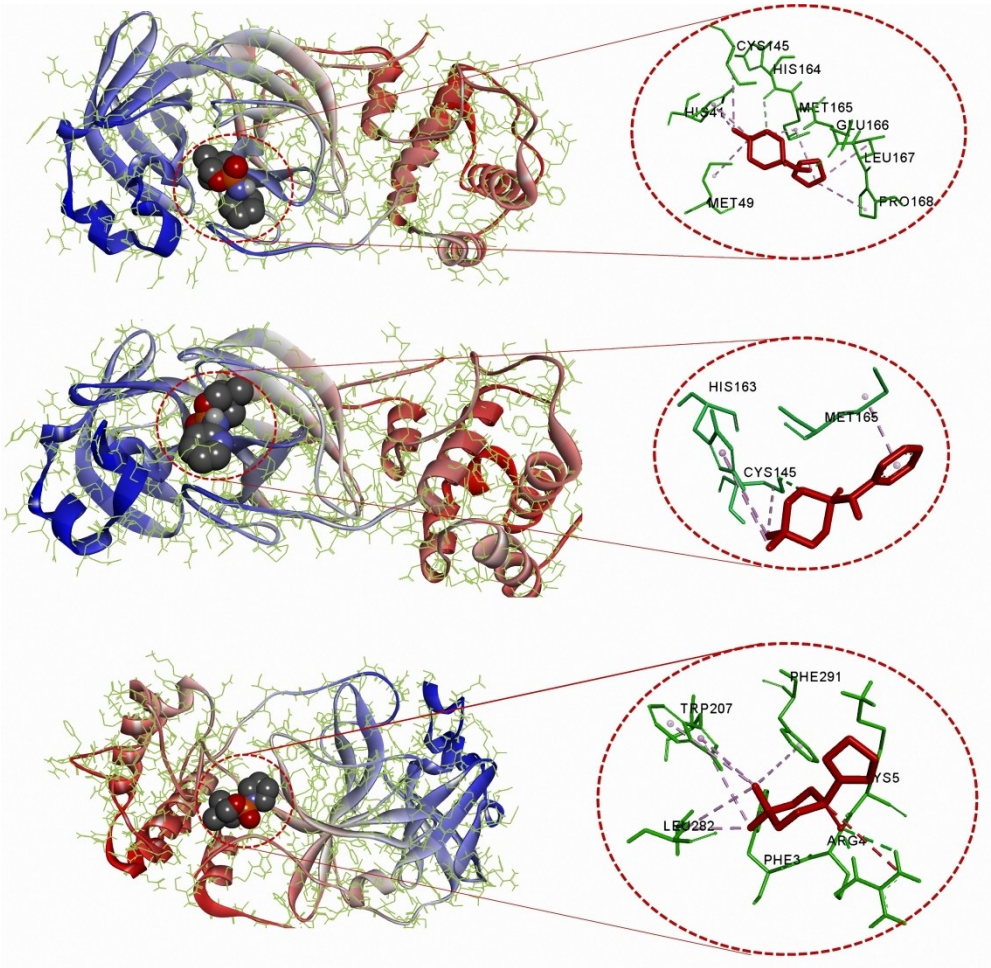

Figure 7. Left: Visual description of the 3-D compounds **1–3** (up to down, respectively) in the best position relative to 6M03 showing the highest negative binding affinity; Right: The 2D representation maps of **1–3** with amino acid sites inside of the active pocket of 6M03.

Table 4. Resulted parameters (kcal/mol) from interaction between ligand and main protease of Autodock 4.2 for the compounds **1–8**.

Compound	1	2	3	4	5	6	7	8
Affinity energy	−6.35	−5.98	−5.47	−6.15	−5. 90	−5.68	−5.13	−5.86

binding energy is for compound **7** bearing the small aliphatic amino substituent with a different value of 1.22 kcal/mole compared to the highest value in **1**. Thus one may conclude that the presence of the aromatic substituents in the amido segment of the studied amidophosphoric acid esters provides a more favorable condition for their biological activities than those bearing the aliphatic amido substituents. Similar results have been obtained in a molecular docking study of some phosphoric triamides, where compounds bearing the aromatic substituents illustrated more negative binding affinity energies compared to those having only aliphatic substituents.[14]

Moreover, a comparison of the various interactions between the compounds **1–8** (Figure S4 and S6) and the structure of the 6M03 protein illustrates that the phosphoryl group is involved in an interaction with some amino acid residues of 6M03 for more compounds. The methyl groups of the esteric ring of structures for all compounds are connected to some amino acid residues of protein by various interactions, and for those including the NH group, amino acid residues of the protein are taking part in interactions with the NH group. However, in the case of the binding energy values of compounds with or without the NH group, one cannot find a specific trend.

IR and NMR study

The presence of the N–H units in **1** and **2** is reflected in the IR spectra at 3200 cm^{-1} and 3161 cm^{-1}, respectively, defining the stretching mode of the N–H unit. Strong bonds related to the P=O stretching modes are found at 1225, 1251 and 1267 cm^{-1}, respectively, for **1–3**, which is in agreement with those

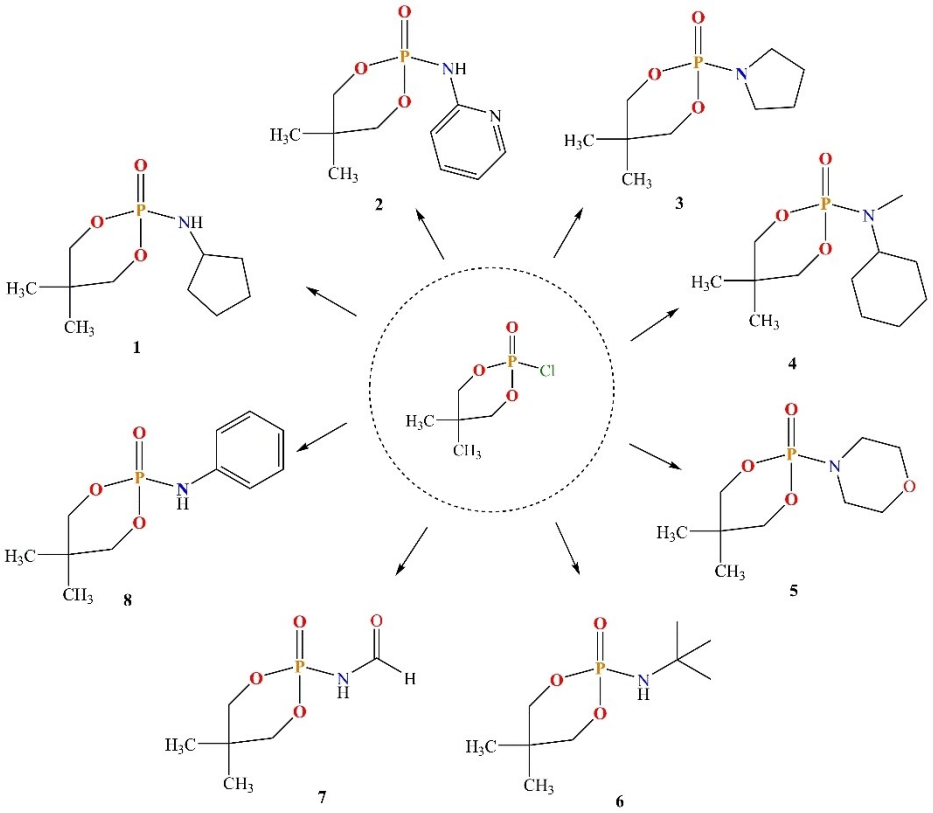

Scheme 2. Chemical structures of the selected compounds **1**–**8** for docking simulation.

observed in similar compounds.[28] P–N frequencies are recorded at 822, 787 and 825 cm^{-1}, respectively for **1**–**3**.

The chemical shifts of 4.25, −6.65 and 3.36 ppm as singlet signals are found in ^{31}P NMR spectra, respectively for **1**–**3**. The ^{31}P signal of **2** is upfield shifted relative to those in **1** and **3** which can be attributed to a larger electronegativity of the phosphorous atom in **2** by the presence of a pyridine ring which is absent in the structures of **1** and **3**.

In the ^{1}H NMR spectra of **1**–**3**, the CH_3 protons of six-membered ring are observed as two singlet signals in the range 0.85–1.15 ppm. For **1** and **2**, the CH_2 protons of six-membered ring are found as two multiplet peaks at 3.81/3.97 and 3.90/4.17 ppm, respectively, whereas for **3**, a multiplet peak at 3.09 ppm is assigned to the CH_2 protons. The related carbon atoms of the CH_3 groups of six-membered ring appear as two singlet signals at the range 19.97–21.45 ppm and the carbon atoms of the CH_2 groups are found as a doublet signal at about 75 or 77 ppm with $^{2}J(P,C) = 5.7$ or 6.8 Hz. The $C(CH_3)_2$ carbon atom is observed as a doublet signal at about 31 ppm with $^{3}J(P,C) = 5.1$ or 6.8 Hz.

For **1**, other chemical shifts of ^{1}H are at 1.58, 1.73, 3.81 and 3.97 ppm as four multiplet peaks which are related to the CH_2 protons of the five-membered ring. The CH proton of five-membered ring also appears as a multiplet peak at 5.14 ppm. This spectrum shows a multiplet signal at 3.40 ppm related to the NH proton. In the ^{13}C NMR spectrum of **1**, the carbon atoms of the CH_2 groups of five-membered ring are found as two singlet signals at 22.86 and 52.64 ppm, and as a doublet signal at 34.06 ppm with $^{3}J(P,C) = 6.0$ Hz.

For **2**, the ^{1}H NMR spectrum shows a multiplet peak at the chemical shift of 4.20 ppm for the N–H proton and the aromatic hydrogens appear as four multiplet peaks in the range 6.88–8.74 ppm. In the ^{13}C NMR spectra, the doublet signals at 110.98 ppm ($^{3}J(C,P) = 7.8$ Hz) and 154.19 ppm ($^{2}J(C,P) = 2.6$ Hz) and also, singlet signals at 116.56, 138.07 and 147.71 ppm correspond to the related aromatic carbon atoms

For the ^{1}H NMR spectrum of **3**, the multiplet signals at 1.76, 3.79 and 4.06 ppm are assigned to the pyrrolidinyl ring protons. The related carbon atoms of the pyrrolidinyl ring in the ^{13}C NMR spectrum are present as two doublet peaks at 25.85 ppm ($^{3}J(C,P) = 9.3$ Hz) and 46.07 ppm ($^{2}J(C,P) = 5.1$ Hz).

Conclusions

In summary, we have reported three new amidophosphoric acid ester compounds **1**–**3**, with the same $[OCH_2C(CH_3)_2CH_2O]P(O)$ segment investigated by spectroscopic and single crystal X-ray diffraction methods. A study of the supramolecular assemblies by using X-ray diffraction and Hirshfeld surface analysis gives a suitable insight of the molecular packing of these compounds. The H…H and H…O/O…H contacts are responsible for the molecular aggregations in the packing of **1**–**3**. However, for **2**, bearing the aminopyridine aromatic substituent, the contacts expand to H…C/C…H and H…N/N…

H besides the H…H and H…O/O…H contacts attributed to the substituent effect. The importance of O…H/H…O contacts including the classical N–H…O=P hydrogen bond interaction in the crystal packings is affirmed by the results of enrichment ratios which show these contacts to be favoured ($E_{OH} > 1$). A biological simulation based on the molecular docking method on the compounds **1–3** and five similar compounds reveals a favourable potentiality to inhibit the M^{pro} of SARS-CoV-2, where the aromatic amido substituents in such compounds increase their biological activities.

Experimental

Spectroscopy

Infrared (IR) spectra were prepared by using a Bruker ALPHA FT-IR spectrometer by a KBr disk. ^{1}H, ^{13}C, $^{31}P\{^{1}H\}$ NMR spectra were recorded by a NMR Bruker Avance 300 MHz spectrometers and chemical shifts were determined relative to TMS (for ^{1}H and ^{13}C) and 85 % H_3PO_4 (for ^{31}P) as external standards.

Syntheses and crystallization

The studied compounds were prepared in a similar method by the treatment of a solution of the commercial starting material $ClP(O)[OCH_2C(CH_3)_2CH_2O]$ (2 mmol) in dry acetonitrile (20 ml) with a solution of related amine (4 mmol, cyclopentylamine, 2-amino-pyridine and pyrrolidine, respectively for **1–3**) in the same solvent (5 ml) at 273 K. The resulted solution was stirred for about 4 h on the stirrer. Then, the solvent was evaporated and the product was washed with distilled water. Single crystals of all three compounds were grown by slow evaporation at room temperature from a solution of the related compound and mixture solvents of CH_3OH/DMF (with volume ratio 3 : 1).

Data for 1: IR (KBr, $\tilde{\upsilon}$, cm^{-1}): 3200 (N–H), 2966, 2893, 1454, 1387, 1309, 1225 (P=O), 1182, 1086, 1013, 949, 822 (P–N), 785, 624, 511, 473; **^{1}H NMR (300.13 MHz, DMSO-d_6, 300.0 K)**: δ = 0.87 (s, 3H, CH_3), 1.01 (s, 3H, CH_3), 1.41 (m, 4H, CH_2), 1.58 (m, 2H, CH_2), 1.73 (m, 2H, CH_2), 3.40 (m, 1H, NH), 3.81 (m, 2H, CH_2), 3.97 (m, 2H, CH_2), 5.14 (m, 1H, CH); **^{13}C NMR (75.47 MHz, DMSO-d_6, 300.0 K)**: δ = 20.48 (s, 1 C, CH_3), 20.97 (s, 1 C, CH_3), 22.86 (s, 2 C, cyclopentyl), 31.44 (d, ^{3}J(C,P) = 5.1 Hz, 1 C, $C(CH_3)_2$), 34.06 (d, ^{3}J(C,P) = 6.0 Hz, 2 C, cyclopentyl), 52.64 (s, 1 C, cyclopentyl), 75.23 (d, ^{2}J(C,P) = 5.7 Hz, 2 C, $2CH_2$); **$^{31}P\{^{1}H\}$ NMR (121.49 MHz, DMSO-d_6, 300.0 K)**: δ = 4.25 (s).

Data for 2: **IR (KBr, $\tilde{\upsilon}$, cm^{-1})**: 3161 (N–H), 2968, 1612, 1597, 1475, 1309, 1251 (P=O), 1215, 1063, 1010, 943, 860, 833, 787 (P–N), 623, 511, 486; **^{1}H NMR (300.13 MHz, DMSO-d_6, 300.0 K)**: δ = 0.85 (s, 3H, CH_3), 1.15 (s, 3H, CH_3), 3.90 (m, 2H, CH_2), 4.17 (m, 2H, CH_2), 4.20 (m, 1H, NH), 6.88 (m, 2H, Ar), 7.61 (m, 1H, Ar), 8.15 (m, 1H, Ar), 8.74 (s, 1H, Ar); **^{13}C NMR (75.47 MHz, DMSO-d_6, 300.0 K)**: δ = 19.97 (s, 1 C, CH_3), 21.45 (s, 1 C, CH_3), 31.73 (d, ^{3}J(C,P) = 6.8 Hz, 1 C, $C(CH_3)_2$), 77.03 (d, ^{2}J(C,P) = 6.8 Hz, 2 C, $2CH_2$), 110.98 (d, ^{3}J(C,P) = 7.8 Hz, 1 C, Ar), 116.56 (s, 1 C, Ar), 138.07 (s, 1 C, Ar), 147.71 (s, 1 C, Ar), 154.19 (d, ^{2}J(C,P) = 2.6 Hz, 1 C, Ar); **$^{31}P\{^{1}H\}$ NMR (121.49 MHz, DMSO-d_6, 300.0 K)**: δ = –6.65 (s).

Data for 3: **IR (KBr, $\tilde{\upsilon}$, cm^{-1})**: 2986, 2846, 1477, 1348, 1267 (P=O), 1207, 1114, 1055, 1009, 970, 922, 874, 825 (P–N), 808, 635, 563, 490, 432; **^{1}H NMR (300.13 MHz, (DMSO-d_6, 300.0 K)**: δ = 0.85 (s, 3H, CH_3), 1.07 (s, 3H, CH_3), 1.76 (m, 4H, CH_2 of pyrrolidinyl ring), 3.09 (m, 4H, CH_2), 3.79 (m, 2H, CH_2 of pyrrolidinyl ring), 4.06 (m, 2H, CH_2 of pyrrolidinyl ring); **^{13}C NMR (75.47 MHz, DMSO-d_6, 300.0 K)**: δ = 20.17 (s, 1 C, CH_3), 21.07 (s, 1 C, CH_3), 25.85 (d, ^{3}J(C,P) = 9.3 Hz, 2 C, pyrrolidinyl ring), 31.46 (d, ^{3}J(C,P) = 5.1 Hz, 1 C, $C(CH_3)_3$), 46.07 (d, ^{2}J(C,P) = 5.1 Hz, 2 C, pyrrolidinyl ring), 75.37 (d, ^{2}J(C,P) = 5.7 Hz, 2 C, $2CH_2$); **$^{31}P\{^{1}H\}$ NMR (121.49 MHz, DMSO-d_6, 300.0 K)**: δ = 3.36 (s).

Crystal structure determination

The details of the crystal data, data collection and structure refinements of **1–3** are given in Table 1. All three measurements were performed on an Rigaku Oxford Diffraction Gemini diffractometer with graphite monochromated Mo $K\alpha$ radiation (λ = 0.71073 Å) using a Sapphire3 CCD detector. Frame integration, scaling and absorption correction using redundant reflections was carried out with *CrysAlisProint*[29] The structures were solved using the charge-flipping method from *Superflip* program[30] with default parameters described elsewhere.[31] The *CRYSTALS* program[32] and *OLEX2* programs[33] were used for the structural refinements. The three structures were refined using two different approaches, one with spherical form factors and the other with aspherical form factors for so-called Hirshfeld atom refinements (HARs)[34] in which electron densities are determined from molecular wavefunctions calculated by quantum mechanical methods and then partitioned into atomic Hirshfeld electron density functions.[35] The calculation of the wavefunctions on the PBE level with a def2-TZVPP basis set and a high SCF convergence threshold were done with the ORCA program.[36–38] The essential step of HAR is to perform a Fourier transformation of the Hirshfeld electron density functions to obtain the related aspherical atomic form factors that are used in the subsequent least-squares refinements. The *NoSpherA2* module in *OLEX2* was used for the aspherical form factor refinements.[39]

For the refinements with spherical form factors H atoms were all located in a difference map, but those attached to carbon atoms were repositioned geometrically. The H atoms were initially refined with soft restraints on the bond lengths and angles to regularize their geometry (C–H in the range 0.93–0.98 Å and N–H in the range 0.86–0.89 Å) and U_{iso}(H) (in the range 1.2–1.5 times U_{eq} of the parent atom), after which the positions were refined with riding constraints.[40]

The structures refined with aspherical form factors were used as starting point for HAR. It was not possible to refine all hydrogen positions completely freely and for a number of these distance restraints set at their approximate neutrons values were used during the refinements. The atomic displacement parameters were refined isotropically. R_F improved in all cases slightly. The final HARed structures were used for the molecular docking studies as it is believed that these give more accurate binding energies than the structures refined with spherical form factors.[15] The molecular graphics were drawn by using the programs PLATON[41] and Mercury.[42]

Hirshfeld surface analysis

The software package *Crystal Explorer* 17.5[43] was utilized to draw the colored graphical maps (Hirshfeld surfaces (HSs)) and plots (fingerprint plots (FPs)) by using the crystallographic information file (CIF) as input. Herein, the HSs are generated based on the d_{norm} distance, a symmetric function of distances from the internal (d_i) and external (d_e) atoms, and shape index.[44,45] The FPs are derived from HS as a 2D grid formed by (d_i, d_e) pairs to facilitate the study of intermolecular interactions. Moreover, the enrichment ratio (E) calculations resulted from the collected data from Hirshfeld surface

analysis is employed for a detailed evaluation of the intermolecular contacts.[25,46]

Molecular docking procedure

The inhibitory effect of the studied compounds **1–3** against the target protein 6M03 (Protein Data Bank identifier; Main Protease (M^{Pro}) of SARS-CoV-2) are investigated by blind molecular docking simulation and the calculated binding energy. The X-ray crystal structure of the 6M03 without any ligand is retrieved from the PDB Data Bank. The software of AutoDock 4.2[47] with AutoGrid 4 was utilized for these calculations. The biological results were obtained by driving the molecular docking and the best position related to ligand and target providing the lowest energy was selected. Heteroatoms and water molecules of the structure of 6M03 were removed using AutoDock tools and hydrogen atoms were placed automatically in the structure of this stripped version of 6M03. All the docking simulations were generated by using a grid box with $100\times100\times126$ Å points and a grid-point spacing of 0.375 Å. The number of evaluations and genetic algorithm runs were set to 100 using a Lamarckian genetic algorithm method. The 2D ligand maps were also generated by the Discovery studio software.[48]

Supporting Information Summary

Supporting information includes Table S1 (selected bond lengths and angles for **1–3**) and Figures S1–S6 (Hirshfeld surface and molecular docking results for the studied compounds).

X-ray crystallography

Deposition Numbers 2110733–2110735, respectively for compounds **1**–**3** contain the supplementary crystallographic data for this paper. These data are provided free of charge by the joint Cambridge Crystallographic Data Center via http://www.ccdc.cam.ac.uk/structures/access structures service.

Acknowledgements

Support of this investigation by Semnan University is gratefully acknowledged.

Conflict of Interest

The authors declare no conflict of interest.

Data Availability Statement

The data that support the findings of this study are available in the supplementary material of this article.

Keywords: Amidophosphoric acid ester · X-ray crystallography · Hirshfeld surface analysis · Molecular docking study · SARS-CoV-2 inhibitor

[1] C. L. Freel Meyers, L. Hong, C. Joswig, R. F. Borch, *J. Med. Chem.* **2000**, *43*, 4313–4318.
[2] T. W. Abraham, T. I. Kalman, E. J. McIntee, C. R. Wagner, *J. Med. Chem.* **1996**, *39*, 4569–4575.
[3] W. Zhang, W. Fan, Z. Zhou, J. Garrison, *ACS Med. Chem. Lett.* **2017**, *8*, 1269–1274.
[4] T. Venkatachalam, P. Samuel, S. Qazi, F. Uckun, *Bioorg. Med. Chem.* **2005**, *13*, 5408–5423.
[5] E. Carletti, J.-P. Colletier, L. M. Schopfer, G. Santoni, P. Masson, O. Lockridge, F. Nachon, M. Weik, *Chem. Res. Toxicol.* **2013**, *26*, 280–289.
[6] M. J. Domínguez, C. Sanmartín, M. Font, J. A. Palop, S. San Francisco, O. Urrutia, F. Houdusse, J. M. García-Mina, *J. Agric. Food Chem.* **2008**, *56*, 3721–3731.
[7] K. Gholivand, A. A. E. Valmoozi, M. Bonsaii, *Pestic. Biochem. Physiol.* **2014**, *112*, 40–50.
[8] C. Huang, Y. Wang, X. Li, L. Ren, J. Zhao, Y. Hu, L. Zhang, G. Fan, J. Xu, X. Gu, *The Lancet* **2020**, *395*, 497–506.
[9] A. Lassoued, A. B. Saad, H. Lassoued, R. Ketata, O. Boubaker, *MedRxiv* **2020**, PPR:R155789.
[10] A. A. Al-Karmalawy, M. A. Dahab, A. M. Metwaly, S. S. Elhady, E. B. Elkaeed, I. H. Eissa, K. M. Darwish, *Front. Chem.* **2021**, *9*, 661230.
[11] G. Sliwoski, S. Kothiwale, J. Meiler, E. W. Lowe, *Pharmacol. Rev.* **2014**, *66*, 334–395.
[12] A. A. Elfiky, *Life Sci.* **2020**, *253*, 117592.
[13] K. Gholivand, A. Barzegari, F. Mohammadpanah, R. Yaghoubi, R. Roohzadeh, A. A. E. Valmoozi, *Polyhedron* **2022**, *221*, 115824.
[14] E. Gholamnezhad, A. Tarahhomi, A. van der Lee, *J. Mol. Struct.* **2022**, *1259*, 132742.
[15] M. Najarianzadeh, A. Tarahhomi, S. Pishgo, A. van der Lee, *Appl. Organomet. Chem.* **2022**, *36*, e6636.
[16] K. Marciniec, E. Chrobak, A. Dąbrowska, E. Bębenek, M. Kadela-Tomanek, P. Pęcak, S. Boryczka, *Biomol. Eng.* **2020**, *10*, 1148.
[17] P. R. Spackman, L. J. Yu, C. J. Morton, M. W. Parker, C. S. Bond, M. A. Spackman, D. Jayatilaka, S. P. Thomas, *Angew. Chem. Int. Ed. Engl.* **2019**, *131*, 16936–16940.
[18] N. Veljkovic, S. Glisic, V. Perovic, V. Veljkovic, *Expert Opin. Drug Discovery* **2011**, *6*, 1263–1270.
[19] M. S. Bozorgvar, A. Tarahhomi, A. van der Lee, *Z. Kristallogr.-Cryst. Mater.* **2020**, *235*, 69-84.
[20] M. Pourayoubi, M. Nečas, M. Negari, *Acta Crystallogr. Sect. C* **2012**, *68*, o51-o56..
[21] A. Tarahhomi, M. Pourayoubi, J. A. Golen, P. Zargaran, B. Elahi, A. L. Rheingold, L. Ramírez, T. Mancilla Percino, *Acta Crystallogr. Sect. B* **2013**, *69*, 260–270.
[22] W. G. Bentrude, W. N. Setzer, E. Ramli, M. Khan, A. E. Sopchik, *J. Org. Chem.* **1991**, *56*, 6127–6131.
[23] A. Tarahhomi, M. Pourayoubi, A. L. Rheingold, J. A. Golen, *Struct. Chem.* **2011**, *22*, 201–210.
[24] M. A. Spackman, J. J. McKinnon, *CrystEngComm* **2002**, *4*, 378–392.
[25] C. Jelsch, K. Ejsmont, L. Huder, *IUCrJ* **2014**, *1*, 119–128.
[26] a) T. S. Cameron, J. Karolak-Wojciechowska, *Acta Crystallogr. Sect. B* **1977**, *33*, 2342–2344; b) T. S. Cameron, Z. Gałdecki, J. Karolak-Wojciechowska, *Acta Crystallogr. Sect. B* **1976**, *32*, 492–496.
[27] M. S. Bozorgvar, A. Tarahhomi, A. van der Lee, *J. Mol. Struct.* **2021**, *1223*, 128942.
[28] A. Tarahhomi, A. van der Lee, B. Ośmiałowski, *Polyhedron* **2019**, *158*, 215–224.
[29] Agilent, **2011**, *CrysAlis PRO*, Version 1.171.138.143c, Agilent Technologies, YarntoOx- fordshire, England.
[30] L. Palatinus, G. Chapuis, *J. Appl. Crystallogr.* **2007**, *40*, 786–790.
[31] A. van der Lee, *J. Appl. Crystallogr.* **2013**, *46*, 1306–1315.
[32] P. Betteridge, J. Carruthers, R. Cooper, K. Prout, D. Watkin, *J. Appl. Crystallogr.* **2003**, *36*, 1487.
[33] O. V. Dolomanov, L. J. Bourhis, R. J. Gildea, J. A. Howard, H. Puschmann, *J. Appl. Crystallogr.* **2009**, *42*, 339–341.
[34] a) S. C. Capelli, H.-B. Bürgi, B. Dittrich, S. Grabowsky, D. Jayatilaka, *IUCrJ* **2014**, *1*, 361–379; b) D. Jayatilaka, B. Dittrich, *Acta Crystallogr. Sect. A* **2008**, *64*, 383–393.
[35] F. L. Hirshfeld, *Theor. Chim. Acta* **1977**, *44*, 129–138.
[36] F. Neese, *Wiley Interdiscip. Rev. Comput. Mol. Sci.* **2012**, *2*, 73-78.
[37] F. Neese, *Wiley Interdiscip. Rev. Comput. Mol. Sci.* **2018**, *8*, e1327.

[38] F. Neese, F. Wennmohs, U. Becker, C. Riplinger, *J. Chem. Phys.* **2020**, *152*, 224108.
[39] F. Kleemiss, O. V. Dolomanov, M. Bodensteiner, N. Peyerimhoff, L. Midgley, L. J. Bourhis, A. Genoni, L. A. Malaspina, D. Jayatilaka, J. L. Spencer, *Chem. Sci.* **2021**, *12*, 1675–1692.
[40] R. I. Cooper, A. L. Thompson, D. J. Watkin, *J. Appl. Crystallogr.* **2010**, *43*, 1100–1107.
[41] A. L. Spek, *Acta Crystallogr. Sect. D* **2009**, *65*, 148–155.
[42] C. Macrae, I. Bruno, J. Chisholm, P. Edgington, P. McCabe, E. Pidcock, L. Rodriguez-Monge, R. Taylor, *J. Appl. Crystallogr.* **2008**, *41*, 466–470.
[43] M. J. Turner, J. J. McKinnon, S. K. Wolff, D. J. Grimwood, P. R. Spackman, D. Jayatilaka, M. A. Spackman, *CrystalExplorer 17.5*, University of Western Australia, Australia, **2017**.
[44] J. J. McKinnon, M. A. Spackman, A. S. Mitchell, *Acta Crystallogr. Sect. B* **2004**, *60*, 627–668.
[45] J. J. McKinnon, D. Jayatilaka, M. A. Spackman, *Chem. Commun.* **2007**, 3814–3816.
[46] M. Sebghati, A. Tarahhomi, A. Kozakiewicz, *ChemSelect.* **2020**, *5*, 185–195.
[47] G. M. Morris, R. Huey, W. Lindstrom, M. F. Sanner, R. K. Belew, D. S. Goodsell, A. J. Olson, *J. Comput. Chem.* **2009**, *30*, 2785–2791.
[48] a) Discovery Studio Modeling Environment. Release 4.5, Dassault Systemes, San Diego, CA, **2015**; b) Discovery Studio Visualizer, v20.1.0.19259; **2009**. Available online: https://discover.3ds.com/discovery-studio-visualizer (accessed on October 2020).

Submitted: April 15, 2022
Accepted: July 7, 2022